Applied Surface Science 606 (2022) 154945

Contents lists available at ScienceDirect

Applied Surface Science

journal homepage: www.elsevier.com/locate/apsusc

Full Length Article

Transition metal single-atom supported on PC_3 monolayer for highly efficient hydrogen evolution reaction by combined density functional theory and machine learning study

Song Lu [a], Jie Cao [a], Yang Zhang [a,b], Fengliu Lou [b], Zhixin Yu [a,*]

[a] Department of Energy and Petroleum Engineering, University of Stavanger, 4036 Stavanger, Norway
[b] Beyonder AS, Kanalsletta 2, 4033 Stavanger, Norway

ARTICLE INFO

Keywords:
Phosphorus carbide (PC_3)
Single-atom catalysts
Hydrogen evolution reaction
Density functional theory
Machine learning

ABSTRACT

It is essential to develop non-precious metal-based alternatives used in hydrogen evolution reaction (HER) due to high cost and scarcity of Pt-based catalysts. Herein, through density functional theory (DFT) calculations, the HER activity over 26 single-atom anchored phosphorus carbide (PC_3) monolayer (TM@PC_3) has been systematically investigated. Results indicate that ΔG_{*H} of V, Fe, Nb, Mo, and Pd@PC_3 are lower than that of Pt (1 1 1) catalyst, with 0.03, −0.03, −0.07, −0.04, and − 0.02 eV, respectively. By imposing the criterion window ($-0.2 \leq \Delta G_{*H} \leq 0.2$ eV), the d band centre (ε_d) for catalysts with excellent HER ability is in the range of − 0.68–0.41 eV. Besides, the five promising HER catalysts follow Volmer-Tafel mechanism. Fe, Nb, and Mo@PC_3 show activation barriers of 0.75, 0.74, and 0.55 eV, lower than that of Pt. Machine learning (ML) was employed to explore the intrinsic relationship between catalytic performance and feature parameters. We demonstrated that the first ionization energy, bond length of TM − H and d band center are more correlated with hydrogen adsorption behaviour. Our work not only predicts that Fe, Nb, and Mo@PC_3 can be substitutes for Pt metal in HER, but also reveals that the intrinsic correlation between catalytic activity and feature parameters by combining DFT and ML investigations.

1. Introduction

Challenges in energy shortage and global warming have driven the society to develop sustainable energy resources [1]. Hydrogen with high mass energy density (~120 MJ/kg) has been regarded as one of the most promising sustainable energy carriers in the future [2,3]. Electrochemical water splitting for the hydrogen evolution reaction (HER) was regarded as an efficient method for hydrogen production [4]. The key for the commercialization of HER is the development of efficient and stable catalysts. To date, the most widely used catalyst for HER is Pt-based due to the low overpotentials. However, the high cost and scarcity have restricted its industrial application [5–7]. To this end, it is a significant challenge to exploit earth-abundant and cost-effective replacement of precious metal-based catalysts for HER application.

In the past few years, two-dimensional materials (2D) have drawn great attention in various catalytic reactions owing to the high surface to volume ratio and unique electronic properties [8–10]. Transition-metal dichalcogenides (MS_2) [11], graphitic carbon nitride (g-C_3N_4) [12], transition-metal carbides/nitrides (MXenes) [13,14], transition-metal boride (MBenes) [15,16], etc. have been investigated as HER catalysts both experimentally and theoretically. Nevertheless, disadvantages such as poor charge transfer, localized active sites and instability, suppress their HER activity. Thanks to the development of nanotechnology, a series of strategies including doping atoms [17,18], engineering nanostructures [19], nanocomposites [20], etc. have been adopted to mitigate these drawbacks and improve their HER performance. For instance, it was reported that substitutional doping of the Mo atoms by Mn, Cr, Fe Ni, Cu can enhance the 1 T-MoS_2 HER activity because of the alteration of the electronic structure by the doping atoms [21]. Geng et al. reported that MoS_2/S-doped g-C_3N_4 layered heterojunction electrocatalysts could tune the electronic structure, enhance charge transfer and expose more active sites of MoS_2 for HER [22]. Li et al. deposited Ru nanoclusters uniformly on nitrogen-doped graphene for alkaline HER. Theoretical study demonstrated that Ru-based nanoclusters could effectively boost water dissociation [23]. Specifically, embedding single metal atom into 2D materials as single-atom catalysts (SACs) have aroused great interest

* Corresponding author.
E-mail address: zhixin.yu@uis.no (Z. Yu).

https://doi.org/10.1016/j.apsusc.2022.154945
Received 26 June 2022; Received in revised form 30 August 2022; Accepted 14 September 2022
Available online 20 September 2022

due to high atom utilization and excellent activity [24–27].

Ultrathin black phosphorus has been fabricated and shown great potential in various fields such as catalysis [28] and electronic devices [29]. Other elements from group V and their compounds including arsenene (As) [30], antimonene (Sb) [31], bismuthine (Bi) [32], black phosphorus carbide (PC) [33] have also been exploited. Among which, PC as novel 2D material has aroused great interest in optical, gas adsorption, energy storage and conversion applications [33–36]. There are different topological configurations such as α and β-PC which have been demonstrated both theoretically and experimentally to possess excellent stability with great potential for electrocatalysis and energy storage [37]. For example, it has been shown experimentally that α-PC has good stability and high hole mobility at room temperature. Chen et al. investigated single metal atom anchored α-PC as SACs in HER by density functional theory (DFT) calculations [17]. They disclosed that Ir embedded α-PC exhibited high physical and thermal stability, as well as the most optimal value of Gibbs free energy for H atom adsorption. Very recently, another phosphorus carbide (PC_3) with P and C atoms in the ratio of 1:3 was predicted to have potential as gas sensor [38]. It is worth noting that the structure of PC_3 is different from α-PC but with good stability. Therefore, it is expected that PC_3 monolayer could be used as single transition metal (TM) atoms support for HER because of the novel geometric and electronic structure.

Recently, the application of machine learning (ML) in catalyst design has shown prominent advantages. For example, it can depict the complicated corelations between descriptors and activity, investigate the importance of each descriptor, and predict the performance of unknown catalysts [39]. In this study, by combined DFT simulation and ML study, we systemically investigated the configuration, stability, electronic structure, HER performance, activation barrier, descriptors and origin of activity of 26 single TM atoms from 3d (Sc, Ti, V, Cr, Mn, Fe, Co, Ni, Cu, Zn), 4d (Zr, Nb, Mo, Ru, Rh, Pd, Ag, Cd) and 5d group (Hf, Ta, W, Re, Os, Ir, Pt, Au) anchored on PC_3 Monolayer. The Gibbs free energies for H atom adsorption on TM@PC_3 catalysts were calculated to screen the catalysts with favourable thermodynamics for HER. It turns out that V, Fe, Nb, Mo, and Pd@PC_3 show comparable low ΔG_{*H} to Pt (1 1 1). Kinetic study demonstrates that V, Fe, Nb, Fe, and Pd@PC_3 follow Volmer-Tafel mechanism, and Fe@PC_3 presents the lowest energy barrier of 0.55 eV. Furthermore, ML was conducted with various models to unravel the intrinsic correlation between electrocatalytic activity and structural and atomic features. The first ionization energy (I), the TM − H bond length (d_{TM-H}) and d band center (ε_d) were regarded as the three most important descriptors for adsorption behaviour based on the mean impact value. This work discloses new novel promising catalysts for HER and reveals the corelation between intrinsic activity and structure as well as atomic features by combined DFT and ML study.

2. Computational methods

The calculations were based on spin polarized DFT method that was implemented in Vienna Ab initio Simulation Package (VASP) code [40]. The projector augmented wave (PAW) was employed to describe interactions of electron–ion. The generalized gradient approximation (GGA) with the Perdew-Burke-Erzerhof (PBE) was adopted to treat the interaction of electronic exchange–correlation energy [41–43]. The kinetic energy cutoff for the planewave basis was set as 500 eV. The convergence criteria for energy and force were set to 10^{-5} eV and 10^{-2} eV/Å. A 3 × 3 supercell with a total of 72 atoms was built based on previous study [38]. A 20 Å vacuum space along the *c* direction was inserted to avoid the interaction from periodic boundary. The parameter for dipole correction was included in our calculations. The Brillouin zone was sampled by the Monkhorst-Pack method for structure relaxation (4 × 4 × 1 *k*-points grid) and electronic structure calculations (8 × 8 × 1 *k*-points grid). The van der Waals interaction was treated by Grimme scheme (DFT-D3) [44]. Solvation effect was included by VASPsol with the dielectric constant of 78.4 for water [45]. Moreover, the ab initio molecular dynamics (AIMD) simulation was carried to explore defective structure stability in an NVT ensemble with a target temperature of 300 K for 12 ps with a time step of 3 fs [46]. Phononpy code based on the density functional perturbation theory (DFPT)-linear response method was chosen to calculate phonon spectra [47]. The climbing image nudged elastic band method (CINEB) was used to search transition state [48].

The formation energy of monolayer PC_3 was calculated by Eq. (1):

$$E_F(PC_3) = E(PC_3) - 3\mu(C) - \mu(P) \quad (1)$$

The defective formation energy (E_F) of single P vacancy was estimated by Eq. (2):

$$E_F(V_P) = E(PC_3 - V_P) + E(P) - E(PC_3) \quad (2)$$

where E(PC_3-V_P), E(P) and E(PC_3) denote the energies of defective PC_3 monolayer, single P atom from stable reference phase and pristine PC_3 monolayer, respectively.

The binding energy (E_b) of TM atoms anchored into the defective PC_3 monolayer was calculated by Eq. (3):

$$E_b = E(TM - PC_3) - E(PC_3 - V_P) - E_{TM} \quad (3)$$

where E(TM-PC_3) and E_{TM} are the energies of TM embedded PC_3, defective E(PC_3-V_P) and single TM atom in vacuum, respectively. According to this definition, negative E_b with a small value indicates that TM atoms can be stably embedded into vacancy.

Moreover, cohesive energy (E_c) was investigated to evaluate whether TM atoms could aggregate on the support, which can be estimated by Eq. (4):

$$E_c = (E_{bulk} - n \times E_{TM})/n \quad (4)$$

where E_{bulk} is the energies of metal crystal.

Therefore, the energy difference (ΔE) between E_b and E_c can be defined by Eq. (5):

$$\Delta E = E_b - E_c \quad (5)$$

With such a definition, the more negative the value of ΔE, the less possibility for aggregation.

There are two steps for the generation of H_2 in acidic condition. In the first step, a proton-coupled electron will form *H, which can be expressed as $H^+ + e^- \rightarrow$ *H (Volmer step), indicating the adsorption of proton on catalytic active site. After that, the formation of H_2 will occur through ($*H + H^+ + e^- \rightarrow H_2$, Heyrovsky step) or ($*H + *H \rightarrow H_2$, Tafel step). Therefore, strong interaction between adsorbed H and catalysts will impede Heyrovsky or Tafel step. In contrast, weak bonding will cause a harsh Tafel step. For an ideal HER catalyst, the Gibbs free energy change of H (ΔG_{*H}) should be close to zero. ΔG_{*H} was calculated by the computational hydrogen electrode (CHE) through Eq. (6) [49]:

$$\Delta G_{*H} = \Delta E_H + \Delta E_{ZPE} - T\Delta S \quad (6)$$

where ΔE_H is the differential hydrogen adsorption energy, ΔE_{ZPE} and TΔS are the differences of zero-point energy and entropy between the adsorption atom and hydrogen in the gas phase, respectively. At pH = 0, the theoretical exchange current *i* based on Norskov's assumption [50] can be expressed as Eq. (7):

$$i = -ek\frac{1}{1 + exp(|\Delta G_{*H}|/k_bT)} \quad (7)$$

where *k* is the reaction rate constant, which was set to 1 as there are no experimental data. k_b and *T* are the Boltzmann constant and temperature, respectively.

The ML process was performed by using commonly used models including gradient boosting regressor (GBR), AdaBoost regressor, linear regression, multiple layer perception and random forest as implemented in the scikit-learn package [51,52].

3. Results and discussion

3.1. Structure, stability, and electronic properties of pristine PC_3 monolayer

As shown in Fig. 1a, PC_3 monolayer have C and P atoms with a ratio of 3:1. The C and P atoms are not coplanar, and the distance between the two planes is 0.67 Å. Besides, there are two different six-atom C-ring and CP-ring, with diameters of 2.82 and 3.10 Å. The calculated lattice parameter *a* of pristine PC_3 monolayer is 5.37 Å, which is well consistent with previous study [38]. The bond length of C − C and P − C are 1.41 and 1.82 Å, respectively. The ∠CCC, ∠CPC and ∠CCP angles in these two rings are 120, 107.15 and 117.68°, respectively.

The formation energy of PC_3 monolayer was calculated to be − 4.80 eV, which is quite close to graphene, indicating good thermal stability. The dynamic stability of PC_3 monolayer was evaluated by the phonon dispersion spectra along the high symmetric points Γ-M−K-Γ, as exhibited in Fig. 1b. Obviously, there are no imaginary frequencies (below the zero), suggesting excellent stability. These confirm the experimental feasibility of PC_3 monolayer.

The electronic structures of PC_3 monolayer were indicated by calculating band structure and project density of state. As plotted in Fig. 1c and d, PC_3 monolayer is a semiconductor with an indirect bandgap of 1.48 eV. The C-*p* state and P-*p* state have a great interaction from conduction to valence bands, evidencing covalent bonding between C and P atoms.

3.2. Structure, stability and electronic properties of TM@PC_3 monolayer

The formation energies of vacancy sites (C and P vacancy) were calculated to be 3.04 and 5.74 eV, which are smaller than that of defective graphene [53]. It also indicates that building C vacancy will be easier than P vacancy in PC_3 monolayer. However, after geometry optimization, the P atom that bonds with the removed C atom will fill C vacancy, forming a four-coordinated P atom in C plane (Fig. 2a). For P vacancy, the vacancy can be preserved without obvious change in structure (Fig. 2b). Therefore, TM atoms will be considered to be only anchored into P vacancy. As depicted in Fig. 2c, one vacancy was occupied by one TM atom. In 3d TM@PC_3, Sc, Ti and V atoms are above the P plane, whereas Cu and Zn@PC_3 are below the C plane. In 4d and 5d TM@PC_3, all TM atoms are located above the P plane. The lattice parameter *a* of TM@PC_3 monolayer were calculated and summarized in Table S1 of Supporting Information (SI). It can be found that the lattice parameter *a* of all TM@PC_3 monolayer increased. Au@PC_3 (5.40 Å) shows the largest increase but still less than 5%. The bond length of the newly formed bond TM − C (d_{TM-C}) are also larger than that of the P − C bond (d_{P-C}) of pristine PC_3 monolayer. The d_{Zr-C} is 2.16 Å, representing the largest increase but less than 18.7% compared with d_{P-C}. These results can be attributed to different atomic radius of TM atoms. In addition, the d_{P-C} in the nearest CP-ring was still the same as that of the pristine PC_3, implying that TM atoms would not influence the activity of surrounding P atoms for HER.

To evaluate the stability of TM anchored monolayer PC_3, the binding energy E_b, the difference between E_b and E_c ($\Delta E = E_b - E_c$) were

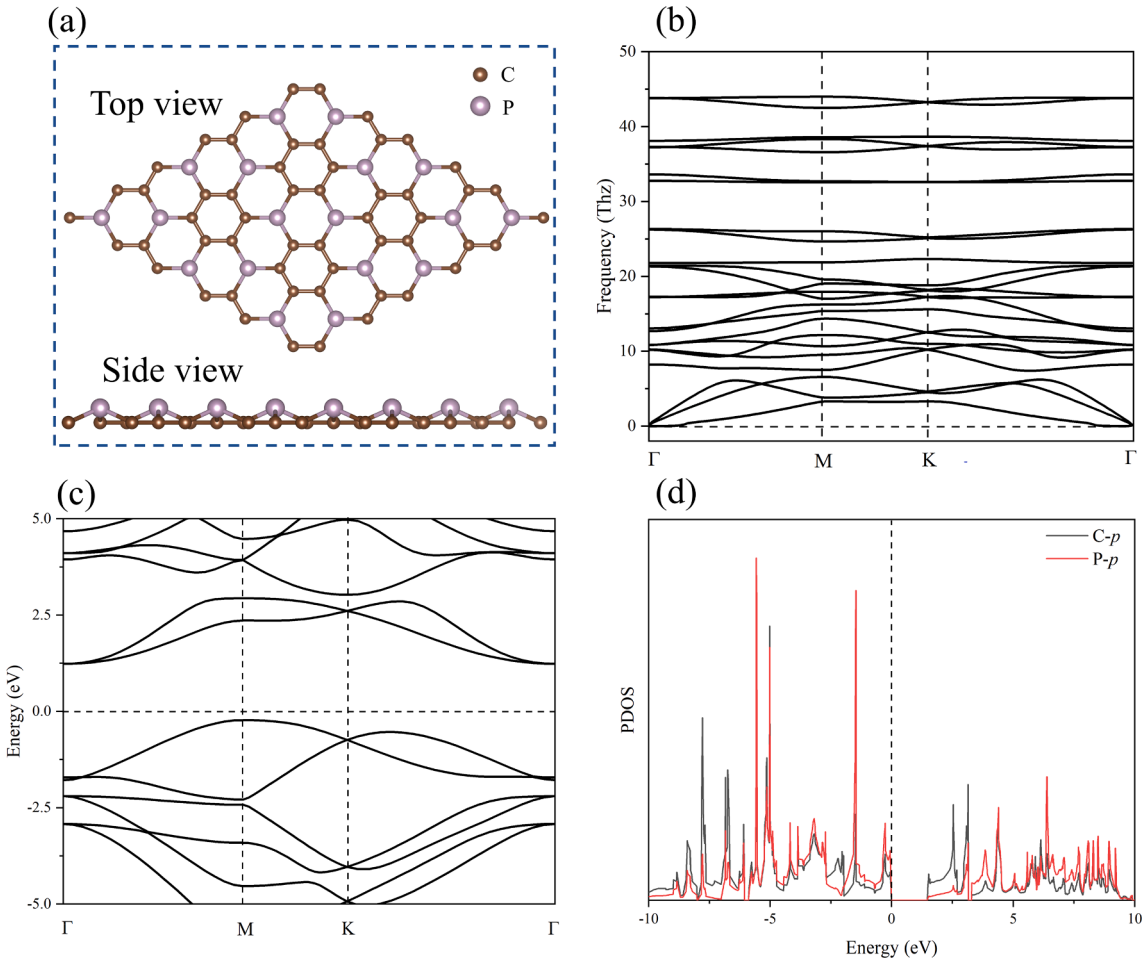

Fig. 1. Schematic structure of 3 × 3 PC_3 monolayer (a); The phonon dispersion curves of PC_3 monolayer along the high symmetry points Γ-M−K-Γ (b); The band structure of PC_3 monolayer (c); The projected density of states (PDOS) of PC_3 monolayer (d); the Fermi energy was set to zero.

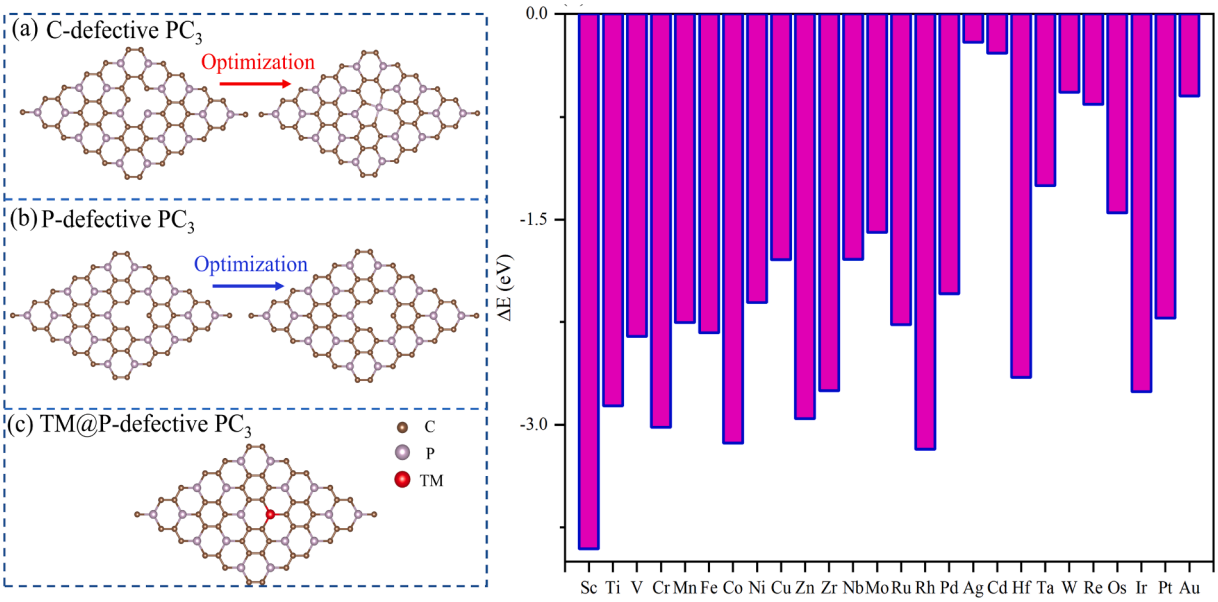

Fig. 2. The structure of C-defective (a), P-defective (b), and TM embedded PC_3 monolayer (c) before and after optimization; The ΔE of all TM@PC_3, where $\Delta E = E_b - E_c$ (d).

calculated and summarized in Table S1. Remarkably, all E_b values are negative, ranging from − 10.13 to − 1.18 eV. The negative values of E_b indicate strong bonding between TM atoms and the support. The single TM atoms could potentially aggerate into clusters on the substrate due to high surface energy. Therefore, the cohesive energies E_c of TM atoms were calculated. It has been widely accepted that the difference between E_b and E_c can be used to describe the degree of aggregation. As exhibited in Fig. 2d, ΔE of all TM@PC_3 are negative, indicating that isolated state of TM atoms is energy favourable in comparison with cluster structure. From the negative values of E_b and ΔE for all structures of TM@PC_3, we can confirm the good stability of TM atoms anchored on P-defective PC_3.

The strong interaction between TM atoms and substrate were also

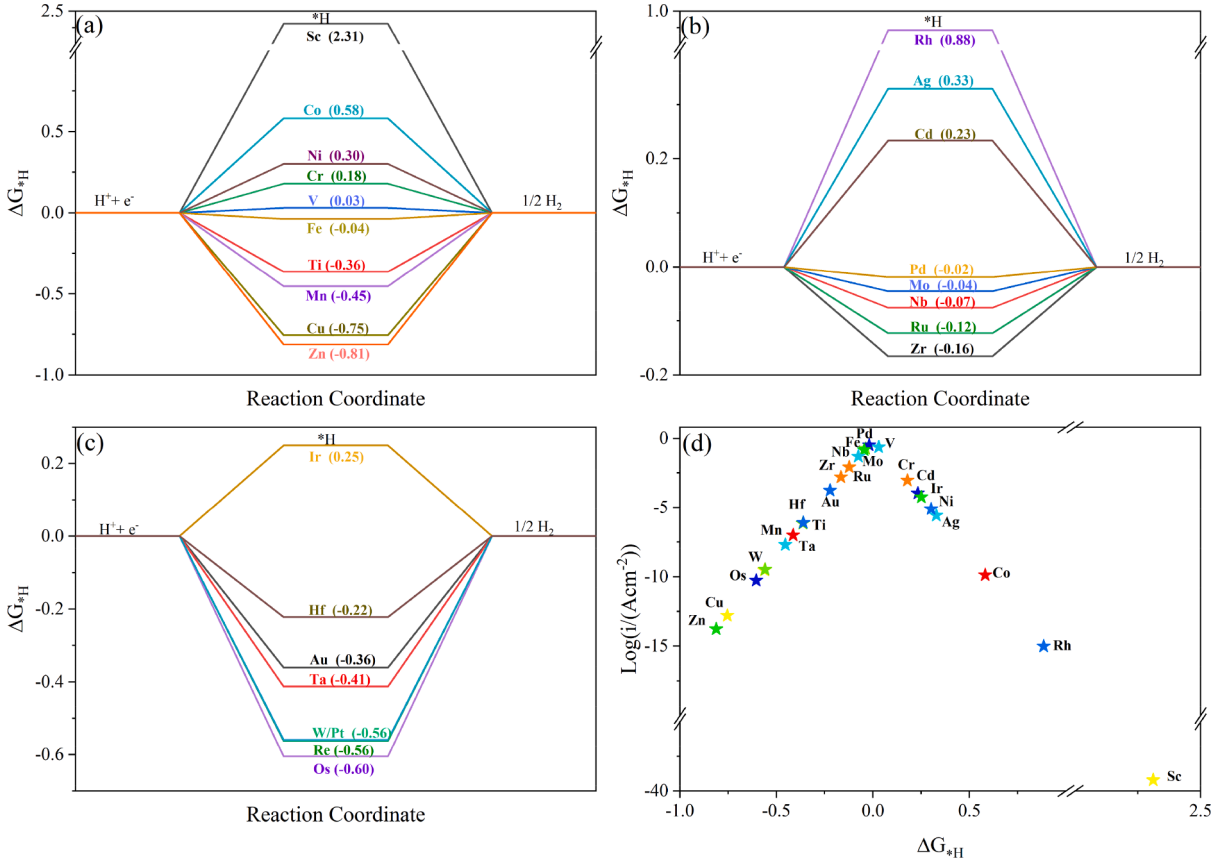

Fig. 3. The Gibbs free energy of H atom adsorption (ΔG_{*H}) on 3d (a), 4d (b) and 5d (c) group atoms embedded PC_3 monolayer; Volcano curve of ΔG_{*H} of TM@PC_3 as a function of the theoretical exchange current i (d).

demonstrated by the charge transfer (Q_e) between them, which could contribute to activating the reactants during catalytic reactions. Bader charge analysis (Table S1) indicates that all TM atoms transfer electrons to the support after TM atoms were anchored into P vacancy due to the electronegativity difference between TM and the coordinated C atoms. Meanwhile, we can also find that Q_e generally decreases with the increase of the atomic number, ranging from 1.59 to 0.55 e for 3d, 1.72 to 0.38 e for 4d, and 1.74 to 0.28 e for 5d group TMs, respectively. Furthermore, the PDOS of TM@PC_3 shows that there are new energy levels near Fermi level (Fig. S1-S3), which is beneficial for electron transport.

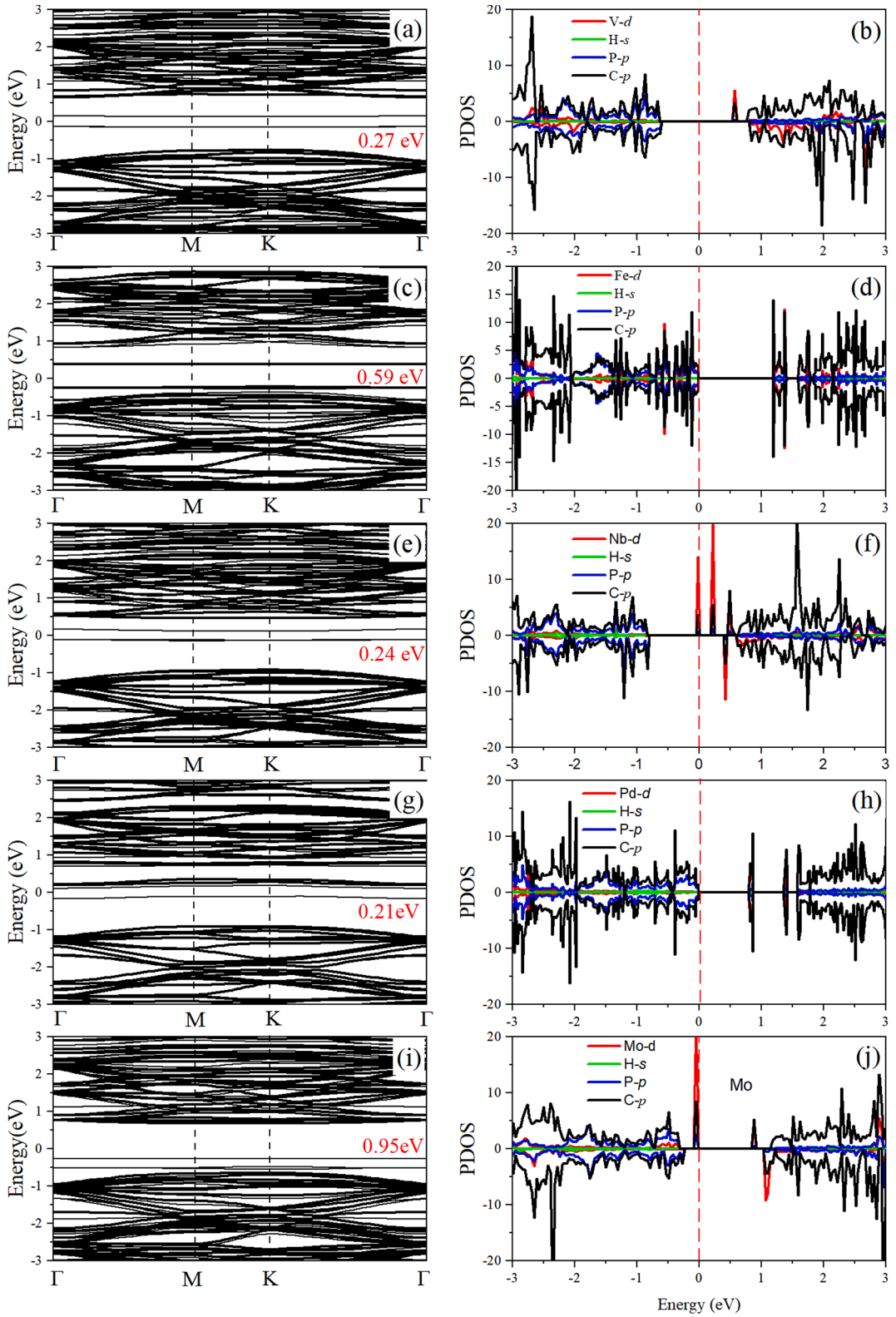

Fig. 4. The band structure and PDOS with H adatom on V@PC_3 (a-b), Fe@PC_3 (c-d), Nb@PC_3 (e-f), Mo@PC_3 (g-h), Pd@PC_3 (i-j).

3.3. HER activity of TM@PC_3 monolayer

ΔG_{*H} between − 0.2 and 0.2 eV is a widely accepted criterion window to screen excellent HER catalysts. The ΔG_{*H} (1/18H coverage) of pristine PC_3 monolayer is 0.68 eV for P sites, while ΔG_{*H} for C sites is quite large at 2.48 eV, suggesting that unmodified PC_3 monolayer is not a good catalyst for HER. After embedding TM atoms, the TM atoms were considered as active sites. For most of the TM@PC_3, H adatom can be adsorbed on top of TM atoms after geometry optimization (Fig. S4-S6). However, For Cu and Zn@PC_3, H adatom prefers to locate at the TM − C bridge sites. For Ni, Pd, Ag, Pt and Au@PC_3, H adatom are at the hollow sites. Different adsorption sites for different SACs evidenced that TM atoms can activate H atoms to different degrees. The HER free energy diagrams of all TM@PC_3 are displayed in Fig. 3a, b and c. For 3d group, only V, Cr and Fe@PC_3 show lower ΔG_{*H} of 0.03, 0.18, −0.04 eV, respectively. For 4d group, more TM atoms including Zr, Nb, Mo, Ru and Pd@PC_3 could exhibit smaller ΔG_{*H}, with − 0.16, −0.07, −0.04, −0.12, −0.02 eV, respectively. For 5d group, however, the ΔG_{*H} of all TM @PC_3 are outside of the criterion window. Therefore, we can conclude that anchoring TM atoms from 5d group on PC_3 monolayer will not be effective for HER. Additionally, given that the anchored TM atom could possibly influence the HER activity of the surrounding C and P atoms, we considered three typical binding sites for H atom adsorption. Take Mo@PC_3 monolayer as an example (Fig. S7), on C_1 site, H atom moved to Mo site after geometry optimization. On C_2 site, ΔG_{*H} is 1.42 eV. On P_1 site, ΔG_{*H} is 0.60 eV, which is close to ΔG_{*H} on P site of pristine PC_3 monolayer. Despite that there is an obvious decrease in ΔG_{*H} on C_2 site, it is still too large compared with ΔG_{*H} on Mo site (−0.04 eV). These results indicate that Mo atom is the only active site in HER.

In addition, the bond lengths d_{TM-H} were summarized in Table S1. The d_{TM-H} of V, Cr, Mn, Zr, Nb, Mo, Ru and Pd@PC_3 vary from 1.50 to 1.92 Å, in accordance with previous study. Furthermore, the intrinsic rate of electrons in the HER at the equilibrium potential can be reflected by the exchange current (i). To compare the HER activity on the TM@PC_3 catalysts, i was plotted against ΔG_{*H}, and a nice volcano curve was obtained (Fig. 3d). The TM atoms close to the volcano peak shows better HER performance of the TM@PC_3 catalysts. It is worth noting that ΔG_{*H} of V, Fe, Nb, Mo and Pd@PC_3 are even lower than that of the state-of-the-art Pt (111) catalyst (−0.09 eV) [50], indicating that these TM atoms anchored on PC_3 monolayer can be excellent SACs for HER.

3.4. Origins of the high HER activity on TM@PC_3

To understand the excellent HER performance of V, Fe, Nb, Mo and Pd@PC_3, the band structure and the DOS of these SACs before and after H atom adsorption were compared (Fig. 4). The bandgap of PC_3 decrease remarkably after anchoring these TM atoms, which could improve the conductivity of the pristine PC_3. Meanwhile, there are new impurity states around Fermi level. For Fe and V@PC_3, it can be assigned to the TM-*d* state, while for Nb@, Mo@ and Pd@PC_3, the impurity states are mainly ascribed to the hybridization of TM-*d* and C-*p* state. For pristine PC_3 monolayer, there are no isolated energy levels generated around Fermi level (Fig. S8), which could not provide stable adsorption state for H atom. Thus, the pristine PC_3 shows poor performance for HER. Remarkably, the partially filed Nb-*d* and Mo-*d* states are formed near Fermi level after anchoring Nb and Mo atoms, which provides an unoccupied state around Fermi level, reducing the electron transport barrier between H atom and the catalysts. Besides, the existence of hybridization between TM@PC_3 and H-*s* state near Fermi level could contribute to the formation of a moderate bonding-antibonding adsorption state for H atoms. Thus, these TM@PC_3 have better catalytic performance for HER than pristine PC_3 monolayer.

Besides, the charge density difference of V, Fe, Nb, Mo and Pd@PC_3 monolayer before and after H adsorption were calculated and shown in Fig. S9. The yellow and cyan colours represent an accumulation and depletion in charge density, respectively. It is obvious that a remarkable charge redistribution occurs between PC_3 monolayer, TM, and H atoms. TM atoms act as electron donor to the surrounding atoms, which increases the unoccupied antibonding states of TM atoms. Therefore, a proper interaction of TM–H bonding contributes to high HER activity.

The catalytic activity is correlated with the electronic structures of active atom sites. Especially, the d-states of TM atom are usually regarded as the activity descriptor (d band center, ε_d). Therefore, ε_d was plotted against ΔG_{*H} in Fig. 5. Obviously, ε_d for 3d, 4d and 5d group TM atoms shift to lower energy level with the increase of atomic number. However, there is no obvious linear relationship between ε_d and ΔG_{*H} on TM@PC_3. Intriguingly, if the criterion window ($-0.2 \leq \Delta G_{*H} \leq 0.2$ eV) is imposed to screen the HER catalysts, the range of d band centre of TM atoms with high HER performance is $-0.68 \leq \varepsilon_d \leq 0.97$ eV and $-3.60 \leq \varepsilon_d \leq 0.41$ eV for 3d and 4d group, respectively. For 5d group, no TM atom is located in the criterion window. Thus, it can be deduced that ε_d of TM@PC_3 catalysts with high HER activity should be in the range of $-0.68 \leq \varepsilon_d \leq 0.41$ eV.

3.5. HER mechanism on TM@PC_3

The activation barrier of HER on V, Fe, Nb, Mo, and Pd@PC_3 was calculated (Fig. 6). Generally, HER is more difficult under alkaline conditions due to additional water molecule dissociation to generate proton. Therefore, only acidic conditions will be considered in this work. The whole HER process can be divided into Volmer–Heyrovsky or Volmer–Tafel step [54]. The Volmer reaction is the initial step that one proton was transferred to the TM@PC_3 surface. We employed one $H_5O_2^+$ cluster (two H_2O groups with one H^+) to describe solvated proton in the solution [20,31]. The minimum energy barrier for Volmer reaction consists of initial step (IS), transition step (TS) and final step (FS), as shown in Fig. 6. One proton breaks away from the $H_5O_2^+$ cluster and adsorbs on the TM sites, indicating the potential catalytic activity of TM atoms towards HER. The calculated energy barriers over V, Fe, Nb, Mo, and Pd@PC_3 are 0.81, 0.75, 0.74, 0.55, and 1.24 eV, respectively.

For H_2 generation, lower energy barrier is preferable, which can be determined by Heyrovsky or Tafel reaction. In Heyrovsky reaction, it is evident that another $H_5O_2^+$ cluster will provide one proton to adsorbed H atom for forming H_2 molecule, which will eventually detach from the TM site. The bond length of adatom H and TM atoms increased slightly, while the proton from $H_5O_2^+$ bonds with the adatom H showing a bond length of around 0.78 Å for H_2 molecule. The energy barriers for Heyrovsky reaction are 1.19, 0.89, 0.97, 0.70, and 1.39 eV on V, Fe, Nb, Mo, and Pd@PC_3, respectively. Obviously, the activation energy of Heyrovsky reaction is larger than that of Volmer reaction on these catalysts. It is also possible that two adjoint adsorbed H atom could combine and generate H_2 molecule (Tafel reaction). In this case, the second H adatom was initially on the top of the nearest P atom. It can be found that H adatom on P atom deviated remarkably from the initial site, while another H atom on TM atom exhibited slight deviation, signifying TM atom having higher HER activity than P atom. Similarly, the bond length of H_2 molecule in the final step are also close to 0.78 Å. Interestingly, the activation barriers for Tafel reaction on these five catalysts are quite low, with 0.37, 0.16, 0.10, 0.24, and 0.14 eV for V, Fe, Nb, Mo, and Pd@PC_3, respectively, which are remarkably lower than that of Heyrovsky reaction. Therefore, the HER on these TM@PC_3 follows Volmer–Tafel mechanism, while the rate determining step is the hydronium adsorption (Volmer). More importantly, the activation energy for HER on these five SACs is comparable or even lower than that of Pt (0.8 eV) [55]. Thus, by combining thermodynamic and kinetic study, we could predict that Fe, Nb, and Mo@PC_3 can be ideal substitutes for Pt metal applied in HER.

The stability of one of the most promising HER catalysts Mo@PC_3 was explored by AIMD simulation with a time step of 3 fs at 300 K for 18 ps. As exhibited in Fig. S10, the total energy shows small fluctuation and the flat structure of Mo@PC_3 appears slightly wrinkle. In addition, it is difficult for Mo atoms diffusion to the neighbouring sites because of high

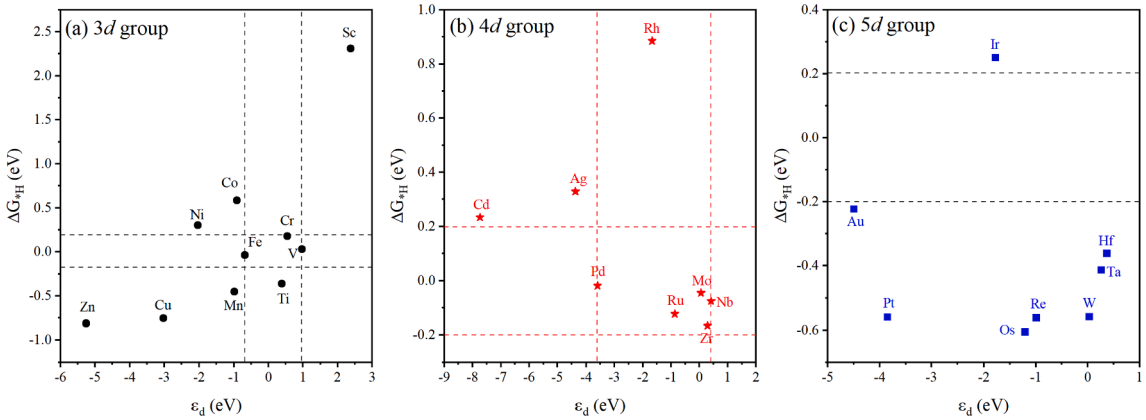

Fig. 5. The d band centre (ε_d) against ΔG_{*H} on 3d (a), 4d (b) and 5d (c) group atoms anchored PC_3 monolayer.

energy barrier at 2.12 eV (Fig. S11), indicating that it is difficult to form Mo aggregates. These results confirm that Mo atom can be stably embedded into the P vacancy, assuring the excellent stability of SACs.

3.6. ML investigation

ML is becoming popular for disclosing data correlations in materials science. Previous studies have demonstrated that the combination of ML and DFT is an efficient way to elucidate the inherent relationship between the descriptor and indicators in catalytic reactions [56–59]. In this work, ΔG_{*H} on TM atoms and the properties of TM atoms were explored by ML. The structural and atomic characteristics (Table S1), including the bond length of TM − C (d_{TM-C}) and TM − H (d_{TM-H}), the binding energy (E_b), the d band center (ε_d), the electronegativity (E_N), the electron affinity (E_A), the first ionization energy (I), the covalent radius (r_{cov}), the charge transfer (Q_e) and the electron number of the d orbital (N_e), are regarded as the descriptors of ΔG_{*H} in ML model training and test. Noteworthily, d_{TM-C}, d_{TM-T}, E_b, ε_d, and Q_e are the chemical properties obtained from DFT calculation, while the others are the intrinsic properties of atoms. Therefore, we presume that the relationship between the catalytic activity and the structural and atomic characteristics on $TM@PC_3$ could be identified by considering 10 descriptors. To identify the correlation between these descriptors, the Pearson correlation coefficient matrix was employed (Fig. 7a). The navy and light-yellow represent those descriptors that are positively or negatively correlated, respectively. It can be found that most descriptors are independent of the catalytic activity. However, some descriptors, for instance, ε_d and N_e, Q_e and N_e, are relatively strongly correlated with a coefficient of − 0.89, consistent with previous study [60].

Although the input data is limited in this work, multiple models, including gradient boosting regressor (GBR), AdaBoost regressor, linear regression, multiple layer perception and random forest were applied and compared (Fig. 7b and Fig. S12). The 26 sets of data were randomly divided into 20 and 6 groups, which were used for ML training and test. By model training and test, a higher coefficient (R^2) and lower root mean squared error (RMSE) are expected. Interestingly, only GBR algorithm exhibits excellent performance with high R^2 of 0.96 and low RMSE of 0.12 eV. This confirms that GBR model is more reliable. Therefore, ΔG_{*H} on $TM@PC_3$ could be satisfactorily predicted by the GBR model. However, the prediction of ΔG_{*H} on unknow HER catalysts will not be included in this work due to limited data.

Furthermore, the relative importance of different descriptors for HER activity was calculated based on the mean impact value (Fig. 8), which could offer further insights into the H atom adsorption ability on $TM@PC_3$. Obviously, the first ionization energy (I), the bond length of TM − H (d_{TM-H}) and d band center (ε_d) are more correlated with H atom adsorption activity, accounting for relative importance of 21.5 %, 18.2 % and 16.3 %, respectively. This result is in accordance with other studies on oxygen evolution/reduction reactions on SACs by DFT and ML study [61]. In contrast, the feature importance of the remaining seven descriptors is relatively low, indicating that these properties have minor effects on H atom adsorption activity. Therefore, it can be concluded that the adsorption behaviour of H atoms over $TM@PC_3$ is mainly determined by the combination of three key descriptors. Besides, it demonstrated that I and d_{TM-H} are better descriptors than the widely used descriptor ε_d to define the HER catalytic activity of $TM@PC_3$. To summarize, the proper adsorption strength of H atom on V, Fe, Nb, Mo, and $Pd@PC_3$ could be explained by the synergistic effect of the first ionization energy, d_{TM-H} and ε_d of TM atoms.

4. Conclusion

In this study, 3d, 4d, and 5d group TM atoms anchored PC_3 monolayer as single-atom catalysts for HER was comprehensively investigated by joint DFT calculation and ML study. The negative formation energy and absence of imaginary frequency in phonon curve demonstrated the structural stability and experimental feasibility of PC_3 monolayer. All the $TM@PC_3$ monolayers are energetically stable. The Gibbs free energy for H adsorption on V, Fe, Nb, Mo, and $Pd@PC_3$ are 0.03, −0.03, −0.07, −0.04, and − 0.02 eV, respectively, lower than that of the Pt (1 1 1) catalyst. ε_d was employed to screen excellent catalysts for HER. It was found that ε_d is located in the range of − 0.68–0.41 eV for high-performance HER catalysts by imposing the criterion window ($-0.2 \leq \Delta G_{*H} \leq 0.2$ eV). The mechanistic study uncovers that V, Fe, Nb, Mo, and $Pd@PC_3$ follow Volmer-Tafel process, which shows activation energies of 0.81, 0.75, 0.74, 0.55, and 1.24 eV, respectively, comparable to that of Pt. Accordingly, $Mo@PC_3$ can be the most promising HER catalyst for the replacement of Pt-based materials. The AIMD simulation demonstrated that Mo atom cannot diffuse to other sites, confirming the excellent stability of SACs. Furthermore, ML was conducted by GBR model to explore the intrinsic correlation between catalytic activity and parameters of the structure and property. Based on the mean impact value, it was found that the HER catalytic activity of $TM@PC_3$ are mainly determined by I, d_{TM-H} and ε_d. Our work paves the way for the design of high-performance catalysts for HER and disclose the relationship between intrinsic activity and features of catalysts.

CRediT authorship contribution statement

Song Lu: Methodology, Investigation, Writing – original draft, Writing – review & editing, Visualization. **Jie Cao:** Investigation, Writing – review & editing. **Yang Zhang:** Investigation, Formal analysis, Writing – review & editing. **Fengliu Lou:** Investigation, Formal analysis, Supervision, Writing – review & editing. **Zhixin Yu:** Conceptualization, Methodology, Validation, Resources, Supervision, Writing – review & editing.

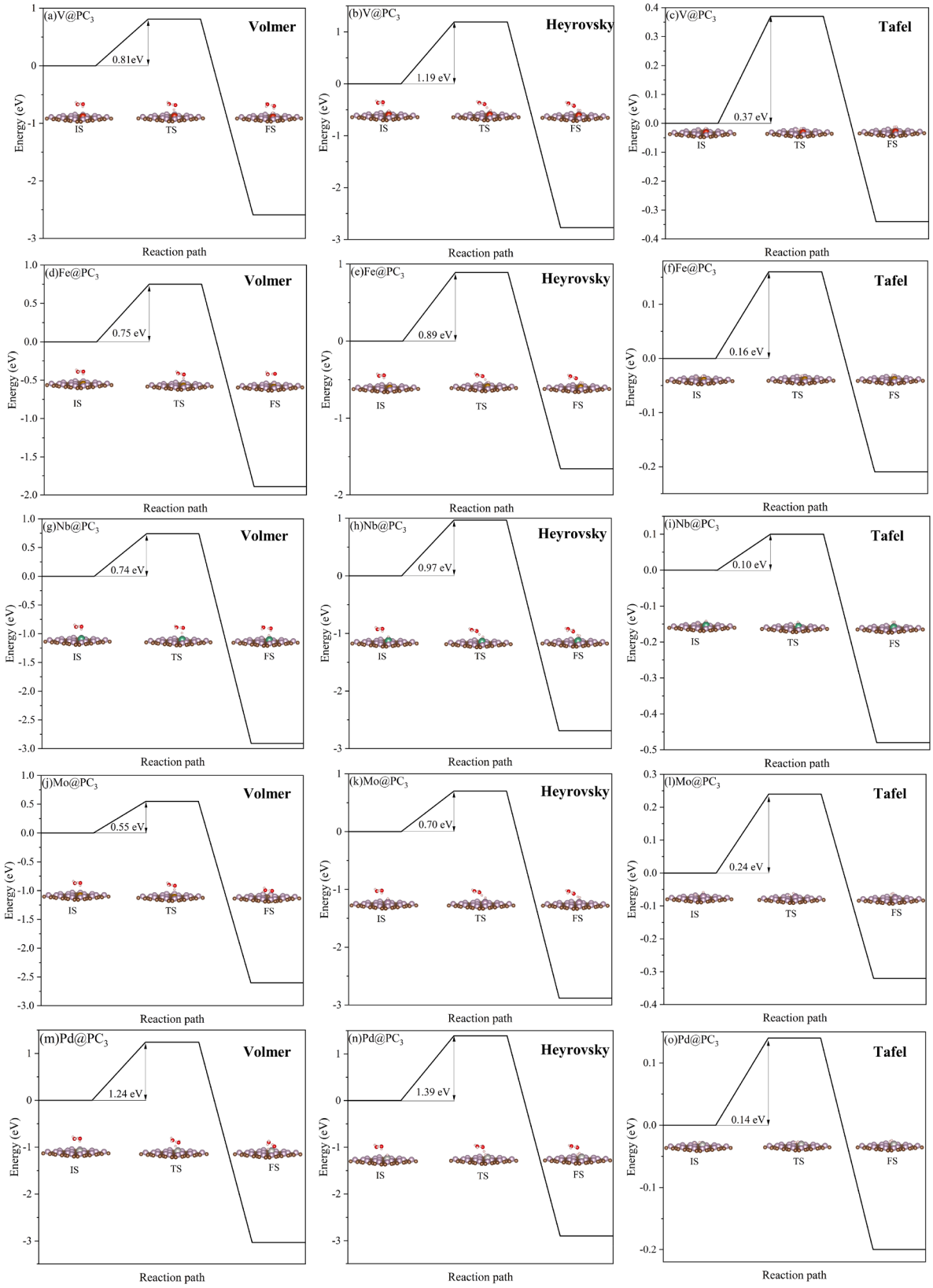

Fig. 6. The minimum energy pathway of Volmer, Heyrovsky and Tafel during HER for $V@PC_3$ (a-c), $Fe@PC_3$ (d-f), $Nb@PC_3$ (g-i), $Mo@PC_3$ (j-l), $Pd@PC_3$ (m-o).

Declaration of Competing Interest

The authors declare that they have no known competing financial interests or personal relationships that could have appeared to influence the work reported in this paper.

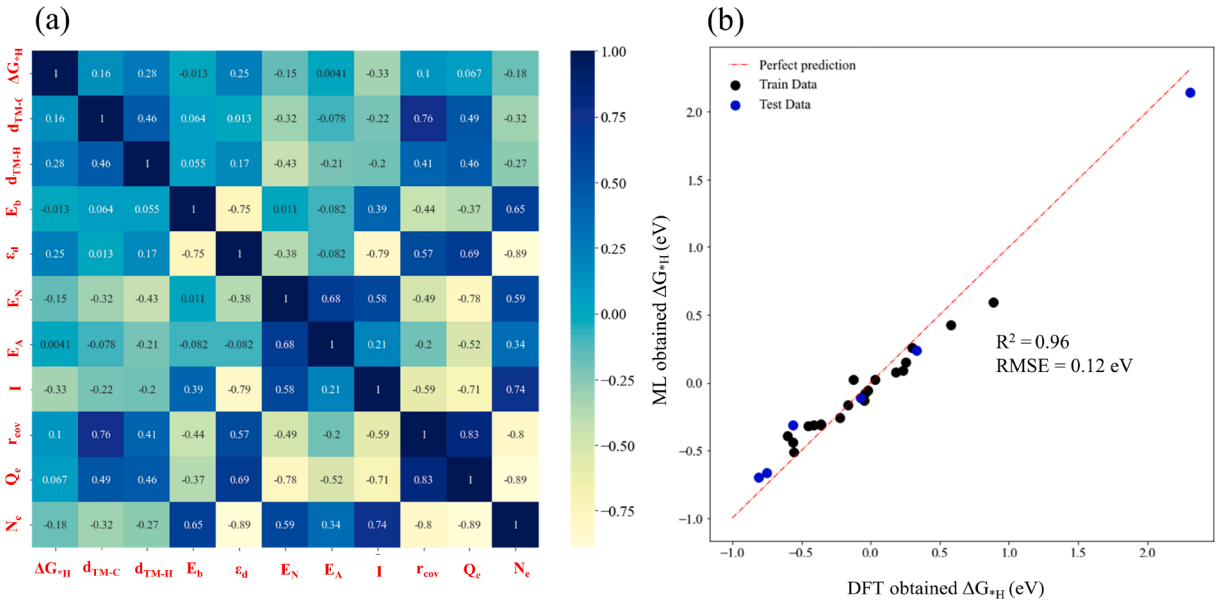

Fig. 7. Pearson correlation heatmap for selected descriptors (a); Comparison between ΔG_{*H} obtained by DFT and GBL model (b).

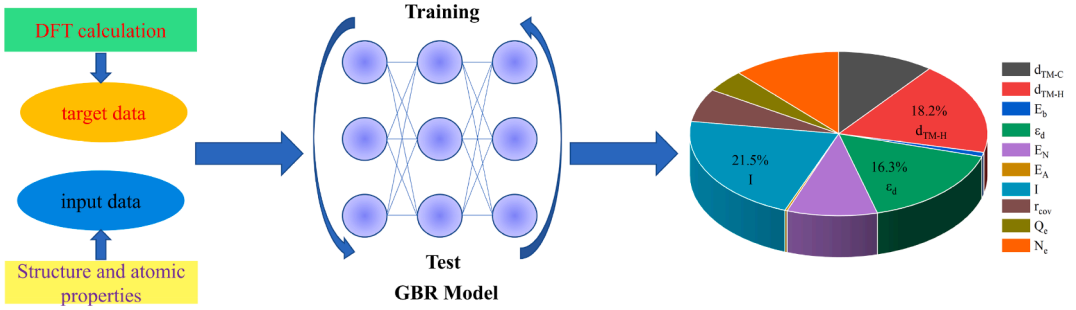

Fig. 8. Brief illustration of the process of machine learning, which can be divided into three steps: data generation, model training and test, and feature importance analysis.

Data availability

Data will be made available on request.

Acknowledgements

This work was supported by the Norwegian Ministry of Education and Research. The computations were performed on resources provided by UNINETT Sigma2 - the National Infrastructure for High Performance Computing and Data Storage in Norway.

Appendix A. Supplementary material

Supplementary data to this article can be found online at https://doi.org/10.1016/j.apsusc.2022.154945.

References

[1] H. Ahmad, S.K. Kamarudin, L.J. Minggu, M. Kassim, Hydrogen from photocatalytic water splitting process: A review, Renew. Sustain. Energy Rev. 43 (2015) 599–610.
[2] A.G. Stern, A new sustainable hydrogen clean energy paradigm, Int. J. Hydrog. Energy 43 (9) (2018) 4244–4255.
[3] N. Mahmood, Y. Ya, J.W. Zhang, L. Pan, X. Zhang, J.J. Zou, Electrocatalysts for Hydrogen Evolution in Alkaline Electrolytes: Mechanisms, Challenges, and Prospective Solutions, Adv. Sci. 5 (2018) 1700464.
[4] N.M. Gupta, Factors affecting the efficiency of a water splitting photocatalyst: A perspective, Renew. Sustain. Energy Rev. 71 (2017) 585–601.
[5] D. Liu, X. Li, S. Chen, H. Yan, C. Wang, C. Wu, Y.A. Haleem, S. Duan, J. Lu, B. Ge, P. M. Ajayan, Y.i. Luo, J. Jiang, L.i. Song, Atomically dispersed platinum supported on curved carbon supports for efficient electrocatalytic hydrogen evolution, Nat. Energy 4 (6) (2019) 512–518.
[6] M.A. Abbas, J.H. Bang, Rising Again: Opportunities and Challenges for Platinum-Free Electrocatalysts, Chem. Mater. 27 (2015) 7218–7235.
[7] M.D. Hossain, Z. Liu, M. Zhuang, X. Yan, G.L. Xu, C.A. Gadre, A. Tyagi, I.H. Abidi, C.J. Sun, H. Wong, A. Guda, Y. Hao, X. Pan, K. Amine, Z. Luo, Rational Design of Graphene-Supported Single Atom Catalysts for Hydrogen Evolution Reaction, Adv. Energy Mater. 9 (2019) 1803689.
[8] R. Hu, G. Liao, Z. Huang, H. Qiao, H. Liu, Y. Shu, B. Wang, X. Qi, Recent advances of monoelemental 2D materials for photocatalytic applications, J. Hazard. Mater. 405 (2021), 124179.
[9] S. Lu, F.L. Lou, Z.X. Yu, Recent Progress in Two-Dimensional Materials for Electrocatalytic CO_2 Reduction, Catalysts 12 (2022) 228.
[10] Y. Wei, R.A. Soomro, X.Q. Xie, B. Xu, Design of efficient electrocatalysts for hydrogen evolution reaction based on 2D MXenes, J. Energy Chem. 55 (2021) 244–255.
[11] S. Li, J. Xiong, X. Zhu, W. Li, R. Chen, G. Cheng, Recent advances in synthesis strategies and solar-to-hydrogen evolution of 1T phase MS2 (M = W, Mo) co-catalysts, J. Mater. Sci. Technol. 101 (2022) 242–263.
[12] Q. Zhu, Z. Xu, B. Qiu, M. Xing, J. Zhang, Emerging Cocatalysts on g-C_3N_4 for Photocatalytic Hydrogen Evolution, Small 17 (2021) 2101070.
[13] G.P. Gao, A.P. O'Mullane, 2D MXenes: A New Family of Promising Catalysts for the Hydrogen Evolution Reaction, ACS Catal. 7 (2017) 494–500.
[14] P. Li, J. Zhu, A.D. Handoko, R. Zhang, H. Wang, D. Legut, X. Wen, Z. Fu, Z.W. Seh, Q. Zhang, High-throughput theoretical optimization of the hydrogen evolution reaction on MXenes by transition metal modification, J. Mater. Chem. A 6 (10) (2018) 4271–4278.
[15] T. Zhang, B. Zhang, Q. Peng, J. Zhou, Z. Sun, Mo_2B_2 MBene-supported single-atom catalysts as bifunctional HER/OER and OER/ORR electrocatalysts, J. Mater. Chem. A 9 (1) (2021) 433–441.

[16] S. Feng, N.X. Miao, J.J. Wang, Hexagonal MBene (Hf_2BO_2): A Promising Platform for the Electrocatalysis of Hydrogen Evolution Reaction, ACS Appl. Mater. Interfaces 13 (2021) 56131–56139.

[17] D. Chen, Z. Chen, X. Zhang, Z. Lu, S. Xiao, B. Xiao, C.V. Singh, Exploring single atom catalysts of transition-metal doped phosphorus carbide monolayer for HER: A first-principles study, J. Energy Chem. 52 (2021) 155–162.

[18] Y. Li, Q. Gu, B. Johannessen, Z. Zheng, H. Liu, C. Li, Y.T. Luo, Z.Y. Zhang, Q. Zhang, H.N. Fan, W.B. Luo, B.L. Liu, S.X. Dou, H.K. Liu, Synergistic Pt doping and phase conversion engineering in two-dimensional MoS_2 for efficient hydrogen Evolution, Nano Energy 84 (2021), 105898.

[19] J. Xie, X. Yang, Y.i. Xie, Defect engineering in two-dimensional electrocatalysts for hydrogen evolution, Nanoscale 12 (7) (2020) 4283–4294.

[20] H.H. Li, Y. Wu, C. Li, Y.Y. Gong, L.Y. Niu, X.J. Liu, Q. Jiang, C.Q. Sun, S.Q. Xu, Design of Pt/t-ZrO_2/g-C_3N_4 efficient photocatalyst for the hydrogen evolution reaction, Appl. Catal. B: Environ 251 (2019) 305–312.

[21] Q. Tang, D.-e. Jiang, Mechanism of Hydrogen Evolution Reaction on 1T-MoS_2 from First Principles, ACS Catal. 6 (8) (2016) 4953–4961.

[22] S. Geng, W.W. Yang, Y.S. Yu, Building MoS_2/S-doped g-C_3N_4 layered heterojunction electrocatalysts for efficient hydrogen evolution reaction, J. Catal. 375 (2019) 441–447.

[23] Y. Li, Y.T. Luo, Z.Y. Zhang, Q.M. Yu, C. Li, Q. Zhang, Z. Zheng, H.K. Liu, B.L. Liu, S. X. Dou, Implanting Ru nanoclusters into N-doped graphene for efficient alkaline hydrogen evolution, Carbon 183 (2021) 362–367.

[24] F. Chen, X.Z. Jiang, L.L. Zhang, R. Lang, B.T. Qiao, Single-atom catalysis: Bridging the homo- and heterogeneous catalysis, Chinese, J. Catal. 39 (2018) 893–898.

[25] X.F. Yang, A. Wang, B. Qiao, J. Li, J. Liu, T. Zhang, Single-Atom Catalysts: A New Frontier in Heterogeneous Catalysis, Acc. Chem. Res. 46 (2013) 1740–1748.

[26] J. Li, M.N. Banis, Z. Ren, K.R. Adair, K. Doyle-Davis, D.M. Meira, Y.Z. Finfrock, L. Zhang, F. Kong, T.K. Sham, R. Li, J. Luo, X. Sun, Unveiling the Nature of Pt Single-Atom Catalyst during Electrocatalytic Hydrogen Evolution and Oxygen Reduction Reactions, Small 17 (2021) 2007245.

[27] J. Zhang, W. Cai, F.X. Hu, H. Yang, B. Liu, Recent advances in single atom catalysts for the electrochemical carbon dioxide reduction reaction, Chem. Sci. 12 (20) (2021) 6800–6819.

[28] Q. Xu, Y. Zhu, T. Xie, C. Shi, N. Zhang, Simultaneous Preparation and Functionalization of Ultrathin Few−layer Black Phosphorus Nanosheets and Their Electrocatalytic OER and HER Performance, ChemCatChem 13 (2) (2021) 592–602.

[29] H.Y. Jun, S.O. Ryu, S.H. Kim, J.Y. Kim, C.H. Chang, S.O. Ryu, C.H. Choi, Inkjet Printing of Few-Layer Enriched Black Phosphorus Nanosheets for Electronic Devices, Adv. Electron. Mater. 7 (2021) 2100577.

[30] Z. Xu, R. Song, M. Wang, X. Zhang, G. Liu, G. Qiao, Single atom-doped arsenene as electrocatalyst for reducing nitrogen to ammonia: a DFT study, PCCP 22 (45) (2020) 26223–26230.

[31] S. Lu, H.L. Huynh, F. Lou, K. Guo, Z. Yu, Single transition metal atom embedded antimonene monolayers as efficient trifunctional electrocatalysts for the HER, OER and ORR: a density functional theory study, Nanoscale 13 (2021) 12885–12895.

[32] S.B. Pillai, S.D. Dabhi, P.K. Jha, Hydrogen evolution reaction and electronic structure calculation of two-dimensional bismuth and its alloys, Int. J. Hydrog. Energy 43 (47) (2018) 21649–21654.

[33] W.C. Tan, L. Huang, R.J. Ng, L. Wang, D.M.N. Hasan, T.J. Duffin, K.S. Kumar, C. A. Nijhuis, C. Lee, K.W. Ang, A Black Phosphorus Carbide Infrared Phototransistor, Adv. Mater. 30 (2018) 1705039.

[34] X. Song, Y. Liu, Y. Yang, W. Li, M. Zhao, Strain-tunable CO_2 storage by black phosphorene and α-PC from combined first principles and molecular dynamics studies, PCCP 21 (36) (2019) 20107–20117.

[35] J. Zhang, G. Yang, J. Tian, Y. Wang, D. Ma, Modulating electronic and optical properties of black phosphorous carbide monolayers by molecular doping, Appl. Surf. Sci. 448 (2018) 270–280.

[36] S. Qi, F. Li, J. Wang, Y. Qu, Y. Yang, W. Li, M. Zhao, Prediction of a flexible anode material for Li/Na ion batteries: Phosphorous carbide monolayer (α-PC), Carbon 141 (2019) 444–450.

[37] J. Guan, D. Liu, Z. Zhu, D. Tománek, Two-Dimensional Phosphorus Carbide: Competition between sp^2 and sp^3 Bonding, Nano Lett. 16 (2016) 3247–3252.

[38] K. Rajput, J.J. He, T. Frauenheim, D.R. Roy, Monolayer PC_3: A promising material for environmentally toxic nitrogen-containing multi gases, J. Hazard. Mater. 422 (2022), 126761.

[39] Z. Li, S. Wang, W.S. Chin, L.E. Achenie, H. Xin, High-throughput screening of bimetallic catalysts enabled by machine learning, J. Mater. Chem. A 5 (46) (2017) 24131–24138.

[40] G. Kresse, D. Joubert, From ultrasoft pseudopotentials to the projector augmented-wave method, Phys. Rev. B 59 (1999) 1758.

[41] P.E. Blochl, Projector augmented-wave method, Phys. Rev. B: Condens. Matter 50 (1994) 17953–17979.

[42] J.P. Perdew, K. Burke, M. Ernzerhof, Generalized Gradient Approximation Made Simple, Phys. Rev. Lett. 77 (18) (1996) 3865–3868.

[43] J.P. Perdew, M. Ernzerhof, K. Burke, Rationale for mixing exact exchange with density functional approximations, J. Chem. Phys. 105 (22) (1996) 9982–9985.

[44] S. Grimme, J. Antony, S. Ehrlich, H. Krieg, A consistent and accurate ab initio parametrization of density functional dispersion correction (DFT-D) for the 94 elements H-Pu, J. Chem. Phys. 132 (2010) 154104–154123.

[45] K. Mathew, R. Sundararaman, K.L. Weaver, T.A. Arias, R.G. Hennig, Implicit solvation model for density-functional study of nanocrystal surfaces and reaction pathways, J. Chem. Phys. 140 (2014) 084106–084114.

[46] G. Kresse, J. Hafner, Ab initio molecular dynamics for liquid metals, Phys. Rev. B 47 (1993) 558.

[47] S. Baroni, S. de Gironcoli, A. dal Corso, P. Giannozzi, Phonons and related crystal properties from density-functional perturbation theory, Rev. Mod. Phys. 73 (2001) 515.

[48] D. Sheppard, R. Terrell, G. Henkelman, Optimization methods for finding minimum energy paths, J. Chem. Phys. 128 (2008), 134106.

[49] J.K. Nørskov, J. Rossmeisl, A. Logadottir, L. Lindqvist, J.R. Kitchin, T. Bligaard, H. Jónsson, Origin of the Overpotential for Oxygen Reduction at a Fuel-Cell Cathode, J. Phys. Chem. B 108 (46) (2004) 17886–17892.

[50] J.K. Nørskov, T. Bligaard, A. Logadottir, J.R. Kitchin, J.G. Chen, S. Pandelov, U. Stimming, Trends in the Exchange Current for Hydrogen Evolution, J. Electrochem. Soc. 152 (2005) J23–J26.

[51] J.H. Friedman, Greedy Function Approximation: A Gradient Boosting Machine, Ann. Stat. 29 (2001) 1189–1232.

[52] F. Pedregosa, G. Varoquaux, A. Gramfort, V. Michel, B. Thirion, O. Grisel, M. Blondel, P. Prettenhofer, R. Weiss, V. Dubourg, Scikit-learn: Machine learning in Python, J. Mach. Learn. Res. 12 (2011) 2825–2830.

[53] A.A. El-Barbary, R.H. Telling, C.P. Ewels, M.I. Heggie, P.R. Briddon, Structure and energetics of the vacancy in graphite, Phys. Rev. B 68 (2003), 144107.

[54] Y.D. Yu, J. Zhou, Z.M. Sun, Novel 2D Transition-Metal Carbides: Ultrahigh Performance Electrocatalysts for Overall Water Splitting and Oxygen Reduction, Adv. Funct. Mater. 30 (2020) 2000570.

[55] E. Skúlason, G.S. Karlberg, J. Rossmeisl, T. Bligaard, J. Greeley, H. Jónsson, J. K. Nørskov, Density functional theory calculations for the hydrogen evolution reaction in an electrochemical double layer on the Pt (111) electrode, PCCP 9 (25) (2007) 3241–3250.

[56] X. Liu, L. Zheng, C. Han, H. Zong, G. Yang, S. Lin, A. Kumar, A.R. Jadhav, N. Q. Tran, Y. Hwang, J. Lee, S. Vasimalla, Z. Chen, S.G. Kim, H. Lee, Identifying the Activity Origin of a Cobalt Single-Atom Catalyst for Hydrogen Evolution Using Supervised Learning, Adv. Funct. Mater. 31 (2021) 2100547.

[57] Y. Ying, K.e. Fan, X. Luo, J. Qiao, H. Huang, Unravelling the origin of bifunctional OER/ORR activity for single-atom catalysts supported on C_2N by DFT and machine learning, J. Mater. Chem. A 9 (31) (2021) 16860–16867.

[58] M. Umer, S. Umer, M. Zafari, M. Ha, R. Anand, A. Hajibabaei, A. Abbas, G. Lee, K. S. Kim, Machine learning assisted high-throughput screening of transition metal single atom based superb hydrogen evolution electrocatalysts, J. Mater. Chem. A 10 (12) (2022) 6679–6689.

[59] X.F. Liu, Y.F. Zhang, W.T. Wang, Y.Z. Chen, W.J. Xiao, T.Y. Liu, Z. Zhong, Z.J. Luo, Z. Ding, Z.F. Zhang, Transition Metal and N Doping on AlP Monolayers for Bifunctional Oxygen Electrocatalysts: Density Functional Theory Study Assisted by Machine Learning Description, ACS Appl. Mater. Interfaces 14 (2022) 1249–1259.

[60] X. Zhao, L. Wang, Y. Pei, Single Metal Atom Catalyst Supported on g-C_3N_4 for Formic Acid Dehydrogenation: A Combining Density Functional Theory and Machine Learning Study, J. Phys. Chem. C 125 (2021) 22513–22521.

[61] H. Niu, X. Wan, X. Wang, C. Shao, J. Robertson, Z. Zhang, Y. Guo, Single-Atom Rhodium on Defective g-C_3N_4: A Promising Bifunctional Oxygen Electrocatalyst, ACS Sustainable Chem. Eng. 9 (9) (2021) 3590–3599.